Inorganic Chemistry
Article
pubs.acs.org/IC

Solid-State Structure and Calculated Electronic Structure, Formation Energy, Chemical Bonding, and Optical Properties of $Zn_4O(FMA)_3$ and Its Heavier Congener $Cd_4O(FMA)_3$

Li-Ming Yang,*[,†] Ponniah Ravindran,[‡] and Mats Tilset*[,†]

[†]Center of Theoretical and Computational Chemistry, Department of Chemistry, University of Oslo, P.O. Box 1033, Blindern, N-0315 Oslo, Norway

[‡]Center for Materials Science and Nanotechnology, Department of Chemistry, University of Oslo, P.O. Box 1033, Blindern, N-0315 Oslo, Norway

Supporting Information

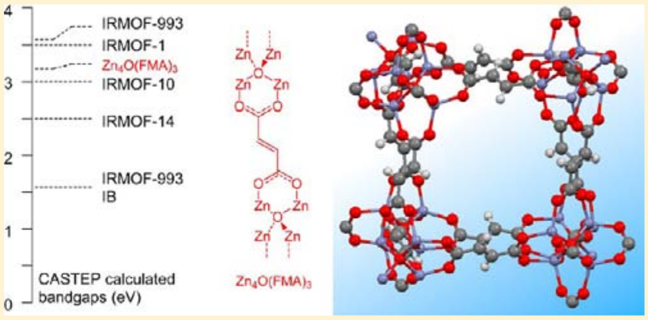

ABSTRACT: The equilibrium solid-state structure of the experimentally synthesized but incompletely characterized $Zn_4O(FMA)_3$ is revised with the help of density functional theory computational methods. The electronic structure, formation energy, chemical bonding, and optical properties of $Zn_4O(FMA)_3$ and its heavier congener $Cd_4O(FMA)_3$ have been systematically investigated. The calculated bulk moduli for $Zn_4O(FMA)_3$ and $Cd_4O(FMA)_3$ are similarly small (and slightly smaller than the previously reported values for MOF-5), indicative of relatively soft materials. Their estimated band-gap values are ca. 3.2 eV (somewhat lower than that of MOF-5, 3.4−3.5 eV), indicating semiconducting character. The optical properties including dielectric function $\varepsilon(\omega)$, refractive index $n(\omega)$, absorption coefficient $\alpha(\omega)$, optical conductivity $\sigma(\omega)$, reflectivity $R(\omega)$, and electron energy-loss spectrum $L(\omega)$ of $M_4O(FMA)_3$ (M = Zn, Cd) were systematically studied. Analysis of chemical bonding reveals that the M−O bonds are largely ionic, with an increase in ionicity from Zn to Cd. The total energy calculations establish that compounds $M_4O(FMA)_3$ have large negative formation energies, ca. −80 and −70 $kJ \cdot mol^{-1}$ for Zn and Cd, respectively. Whereas $Zn_4O(FMA)_3$ has already been synthesized, the results suggest that the heavier congener $Cd_4O(FMA)_3$ might be experimentally accessible.

I. INTRODUCTION

Metal−organic frameworks (MOFs)[1,2] constitute a rather new class of materials that possess well-defined solid-state network structures consisting of metal atom or cluster cornerstones (most often metal oxo clusters) linked by organic ligands. Owing to the porosities and high specific surface areas of many MOFs, they are interesting materials for various applications in catalysis, gas adsorption and storage (e.g., energy gases, H_2, CH_4, CO_2, etc.), selective separation, sensing, molecular recognition, and more.[3]

One fundamental challenge in the realm of MOF chemistry is to obtain reliable, preferably high-resolution, crystal structures for the pure phases. This is often not possible for many MOFs, which are typically synthesized under solvothermal conditions and so will include guest molecules, solvents or others, that are accommodated in the pores. Computational simulations and optimizations may provide a valuable supplement to improving the structural understanding of MOFs, many of which remain incompletely or inaccurately described based on the available experimental structure data.

Recently, Chen and co-workers[4] synthesized the non-interpenetrated MOF $Zn_4O(FMA)_3$ (FMA = fumarate) with high rigidity and porosity, which makes it interesting for gas storage. The FMA linker is readily available and inexpensive compared to many other organic linkers and is also among the smaller MOF linkers available; it has found extensive uses in homolinked[4−10] and heterolinked[11−18] MOFs. Nevertheless, the finer structural details of $Zn_4O(FMA)_3$ cannot be discerned from the experimental crystallographic data. A recent computational study on $Zn_4O(FMA)_3$ did not give further structural details.[19] Here, we perform a computational investigation on $Zn_4O(FMA)_3$ and its Cd congener, not yet experimentally available, to demonstrate how computations can aid and enhance structure determinations of MOFs.

The MOF $Zn_4O(FMA)_3$ has the same topology as the well-known IRMOF series,[20] in which the prototypical MOF-5 with its benzene-1,4-dicarboxylate (BDC) linker is particularly well-known. FMA is a rather small linker, which brings the cornerstone clusters closer together, with the potential to significantly affect the electronic properties of the MOF compared to other linkers. It is therefore of particular interest

Received: September 4, 2012
Published: March 28, 2013

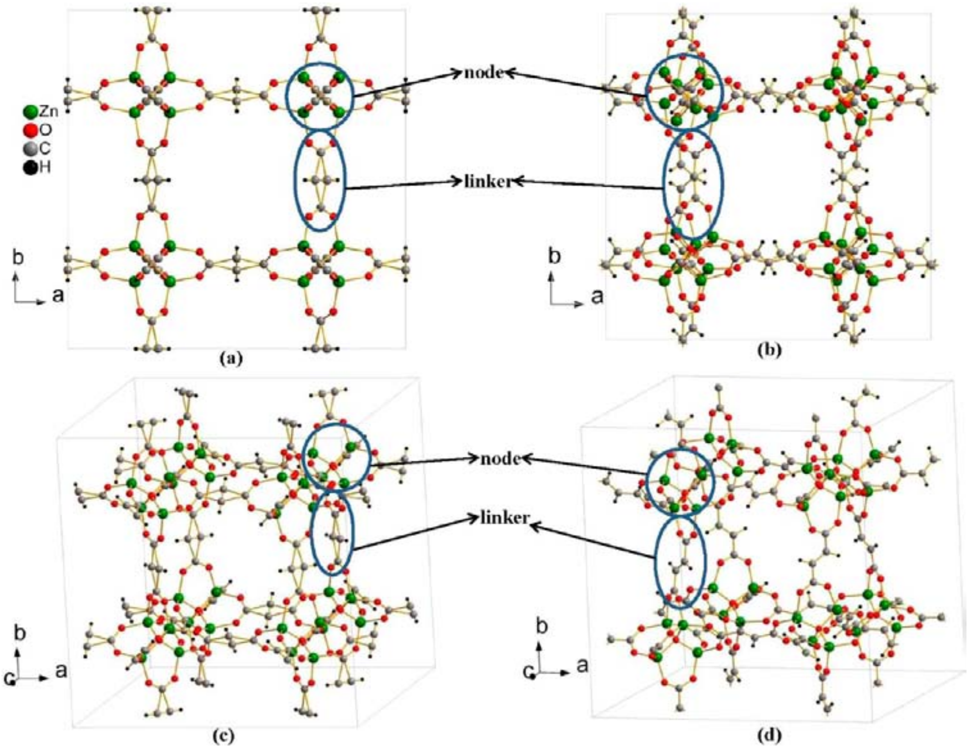

Figure 1. Depictions of the crystal structure of $Zn_4O(FMA)_3$: (a) and (c) based on the experimental data,[4] top and side views; (b) and (d) based on the present computations, top and side views. Note that parts a and c are in the fcc symmetry $Fm\bar{3}m$ (No. 225), whereas parts b and d are in the sc symmetry $P23$ (No. 195). The significant differences in the nodes and linkers are circled.

to compare the crystal and electronic structures of $Zn_4O(FMA)_3$ with MOF-5.

Chen and co-workers[4] reported the crystal structure of $Zn_4O(FMA)_3$, which was refined in space group $Fm\bar{3}m$ (No. 225) of cubic symmetry with the lattice parameter $a = 21.639$ Å. Metric data reported in the paper and its Supporting Information (SI) included only Zn−O distances and O−Zn−O angles for the cornerstone zinc clusters. Details of the linker geometry could not be discerned because the two central FMA C atoms were not located in the crystallographic analysis.[21] Inspection of the CIF file with the *Mercury 3.0* program[22] indeed showed that the structural details of the linker were poorly resolved. This is likely due to disorder and poorly located atomic positions. In addition, it is clear that the zigzag conformation of the carbon skeleton of the FMA cannot possibly give rise to the idealized symmetries of the face-centered-cubic (fcc) lattice but rather to a simple cubic (sc) one. We note that it is quite common in MOF characterization that X-ray data are refined in space groups of too high symmetry; the artificially high symmetry may result from the disorder problems, and the finer details of the linker will necessarily be inaccurately reproduced. To illustrate this for the MOF under consideration here, the crystallographic CIF file erroneously shows the central C═C bond to be perpendicular to the axis between the two carboxylate C atoms; the apparent central C═C bond distance in the linker is 1.065 Å [much shorter than a typical C═C double bond of 1.36 Å or the C═C double bond in fumaric acid, determined by X-ray diffraction as 1.315(7) Å],[23] and the apparent ═HC−C(carboxylate) distance of 1.832 Å obtained when viewing the reported CIF file with the *Mercury 3.0* program[22] is unrealistically long [1.490(5) Å in fumaric acid[23]].

Alternatives to the diffraction analysis are needed to describe this material well, in particular concerning the nature of the linker. Here, we describe a comprehensive theoretical study on the crystal structure, formation energy, electronic structure, chemical bonding, and optical properties of $M_4O(FMA)_3$ (M = Zn, Cd) using density functional theory (DFT) calculations with the generalized gradient approximation (GGA)−Perdew, Burke, and Ernzerhof (PBE) functional, as implemented in the Vienna ab initio simulation package (VASP). The optical properties of $M_4O(FMA)_3$ were calculated using the CASTEP module of the *Material Studio* program. The use of computational methods to optimize and predict MOF structures and to evaluate their various properties, including mechanical, optical, and electronic properties, has recently become an important supplement to experimental approaches.[24−37]

II. COMPUTATIONAL DETAILS

The VASP[38−41] was used for total-energy calculations to study the structural stability and to establish equilibrium structural parameters. The GGA[42−44] includes the effects of local gradients in the charge density for each point in the materials and generally gives better equilibrium structural parameters than the local density approximation. Hence, the GGA functional was used for all calculations. The projector-augmented-wave[45,46] and PBE[44] pseudopotentials based on GGA were used to describe the ion−electron interactions. A criterion of 0.01 meV atom^{-1} was placed on the self-consistent convergence of the total energy, and all calculations were made with a plane-wave cutoff of 500 eV, which ensures that absolute energies converge to within a few millielectronvolts per formula unit. This has been tested to be accurate and reliable for the $M_4O(FMA)_3$ (M = Zn, Cd) systems under consideration here. Brillouin-zone integration was performed with a Gaussian broadening of 0.2 eV during all relaxations. The conjugated-gradient algorithm based on Hellmann−Feynman forces was used to relax the ions into their instantaneous equilibrium positions. The forces and stress tensors were used to determine the

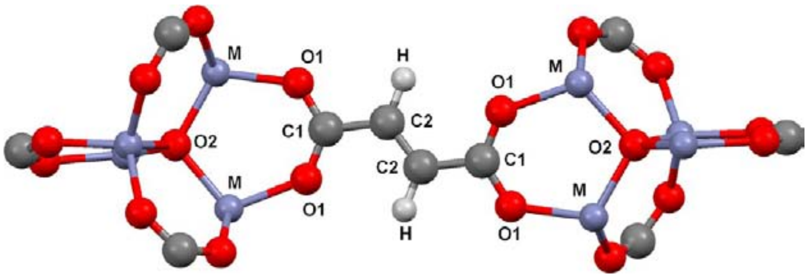

Figure 2. Atom-labeling scheme for $M_4O(FMA)_3$ (M = Zn, Cd).

search directions to identify the ground state (i.e., the total energy is not taken into account). This algorithm is very fast and efficient when the initial structures are far away from the ground state. Forces on the ions were calculated using the Hellmann−Feynman theorem as the partial derivatives of the free electronic energy with respect to the atomic positions and adjusted using the Harris−Foulkes correction to the forces. The atoms were relaxed toward equilibrium until the Hellmann−Feynman forces were less than 10^{-3} eV $Å^{-1}$.

Because we deal with a rather large system (280 atoms per primitive cell), the $\mathbf{\Gamma}$ point alone is sufficient for sampling the Brillouin zone during geometry optimization. However, in order to arrive at an accurate band structure, a sufficient number of **k** points were used for band-structure calculations. The density of state (DOS) calculations were performed on the fully optimized structure with only $\mathbf{\Gamma}$ point alone. However, the DOS was calculated in a fine energy grid (801 points) due to the narrow band features so as to visualize DOS correctly.

To assess the bonding characteristics, bond overlap population (BOP) values were analyzed with an ultrasoft pseudopotential estimated on the basis of the Mulliken population analysis, as implemented in the CASTEP code.[47] In order to understand the chemical bonding and interactions between constituents in $M_4O(FMA)_3$, charge density, charge transfer, and electron localization function (ELF)[48−51] analyses were also performed based on the results obtained from VASP calculations. Optical properties, including the dielectric function, absorption coefficient, reflectivity, refractive index, optical conductivity, and energy loss function, were calculated for $M_4O(FMA)_3$ using the CASTEP code. The band structures were calculated with an ultrasoft pseudopotential using CASTEP. The methods that were used for calculation of the optical properties and band structures have been proven to be reasonable and compared favorably with the corresponding experimental spectra in previous contributions from our and other groups.[52−62]

III. RESULTS AND DISCUSSION

A. Structural and Topological Aspects of $M_4O(FMA)_3$ (M = Zn, Cd). $Zn_4O(FMA)_3$ is a member of the isoreticular IRMOF series available through the reticular synthesis approach proposed by Yaghi and co-workers.[63,64] Various depictions of the structure of $Zn_4O(FMA)_3$ are given in Figure 1. The structure topology is similar to the well-known MOF-5 (IRMOF-1);[20] both have oxo-centered Zn_4O tetrahedra as nodes linked by organic dicarboxylates. Replacement of the linker BDC in MOF-5 with FMA provides $Zn_4O(FMA)_3$.

The conventional cell (Figure 1a,c) of $Zn_4O(FMA)_3$ was described by Chen and co-workers[4] after structure refinement in the high-symmetry fcc space group $Fm\bar{3}m$ (No. 225) with the lattice parameter a = 21.639 Å and with eight formula units. The primitive cell of Chen's $Fm\bar{3}m$ structure involved in our calculations includes two nodes and six linker molecules, corresponding to two $Zn_4O(FMA)_3$ formula units. The inequivalent crystallographic sites in the fcc symmetric $Zn_4O(FMA)_3$ includes one type of Zn, two types of O, two types of C, and one type of H occupying 32f, 8c, 96k, 48g, 48h, and 48h Wyckoff positions, respectively. We found, as expected, that it was not possible to optimize the structure of $Zn_4O(FMA)_3$ (based on the experimental data given in the SI provided by Chen and co-workers[4]) within the fcc symmetry (Figure 1a,c). Rather, optimizations arrived at the sc symmetry [$P23$ (No. 195)] structure (Figure 1b,d) with considerably altered linkers and nodes. This sc structure includes 26 types of atoms: four types of Zn, 10 types of O, eight types of C, and four types of H occupying 12j, 12j, 4e, 4e, 12j, 4e, 4e, 12j, 12j, 12j, 12j, 12j, 12j, 12j, 12j, 12j, 12j, 12j, 12j, 12j, 12j, 12j, 12j, 12j, 12j, and 12j Wyckoff positions, respectively. The number of atoms in the primitive cell is now 280 because of the lowering of the symmetry. From a comparison of parts a and c with parts b and d of Figure 1, one can clearly see the differences between the experimental structure and the structure obtained from our structural optimization. Clearly, the computational simulation provides a crucial confirmative tool to supplement or correct incomplete or erroneous experimental data for such complex crystal structures.

The optimized crystal structure of $Zn_4O(FMA)_3$ was used, after replacement of Cd for Zn, as the input for optimization of the heavier congener $Cd_4O(FMA)_3$. The latter is predicted to have the same structural framework and topology but with somewhat different lattice parameters because of the difference in the ionic radii of Zn and Cd.

Among the 26 Wyckoff positions in the unit cell of $M_4O(FMA)_3$ in the sc symmetry, some atoms have similar or even identical chemical environments. These atoms are grouped together, and one of them is taken as a representative example for the discussion of the electronic structure and chemical bonding. The resulting six atom types are shown and labeled in Figure 2.

B. Structural Optimization of $M_4O(FMA)_3$ (M = Zn, Cd) from Total-Energy Calculation. The reported crystal structure data for $Zn_4O(FMA)_3$[4] (SI, CIF file) was imported into the *Materials Studio* software package for visualization. The atomic positions of the linker atoms were adjusted to produce a reasonable input structure for the calculations. The computed ground-state structure was then obtained from this initial structure by full geometry optimization; i.e., the atom positions and cell parameters were completely relaxed without any symmetry constraints. This fully optimized structure of $Zn_4O(FMA)_3$ was used as a starting structure for $Cd_4O(FMA)_3$ by replacing the Zn atoms with Cd before new structural optimization was made.

The first stage of the structural optimization was achieved by relaxing the atomic positions globally using the force-minimization technique with the lattice constant (a) and cell volume (V) fixed to the experimentally reported values. The theoretical ground-state volume was then determined from the minimum in the total energy by varying the cell volume within

±10% of the experimentally determined volume with complete relaxation of atoms in each volume step. The calculated total energy as a function of the volume was fitted to the so-called equation of state (EOS) to calculate the bulk modulus (B_0). The bulk mechanical properties of MOFs are important to many applications, and the bulk modulus is one key mechanical parameter that needs to be assessed.[35,65] In order to cross-check the calculated B_0 values, the $E-V$ data were fitted into three different EOS, i.e., Murnaghan (MEOS),[66] Birch–Murnaghan (BMEOS),[67] and universal (UEOS) equation of states.[68] The bulk moduli obtained from the $E-V$ curve using MEOS, BMEOS, and UEOS are 12.72, 12.89, and 12.79 GPa for M = Zn and 8.88, 8.63, and 8.84 GPa for M = Cd. The B_0 values imply that compounds $M_4O(FMA)_3$ are relatively soft materials. The bulk modulus decreases slightly from M = Zn to Cd, probably because of an increase in the equilibrium volume. There are no experimentally measured bulk modulus values available for these compounds with which to compare our results. However, the following trend is seen in B_0 data (average of the three EOS) taken from the present contribution and our previously reported calculations of various zinc-based IRMOFs (see Scheme 1 for chemical structures): Zn-IRMOF-1,[69] 15.4; Zn-IRMOF-10,[70] 9.1; Zn-IRMOF-14,[71] 10.2; Zn-IRMOF-993,[72] 15.9; $Zn_4O(FMA)_3$, 12.8 GPa. It is evident that short and rigid linkers promote mechanical stability.

Scheme 1

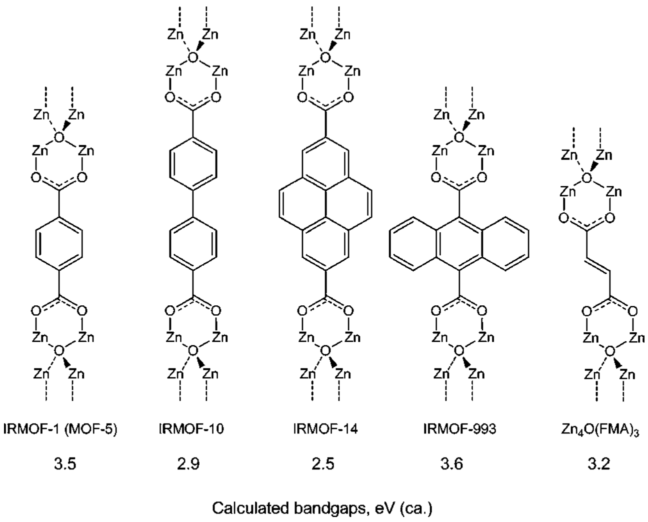

A comparison between the reported structural data based on experimental measurements and the computational results can be found in Tables 1 and 2 and in Figure 3. Table S1 (SI) gives a complete list of the computationally determined atomic positions (x, y, z). The optimized equilibrium lattice parameters of $M_4O(FMA)_3$, along with the corresponding experimental values of $Zn_4O(FMA)_3$, are collected in Table 1. The lattice parameter of $Zn_4O(FMA)_3$ in the present work (21.806 Å) is in good agreement with the experimental value[4] (21.639 Å). For $Cd_4O(FMA)_3$, the lattice parameter (21.933 Å) is slightly greater than that of $Zn_4O(FMA)_3$, as expected because of an increase in the ionic radius from Zn to Cd. In Table S1 in the SI, considerable discrepancies between the experimental and computational results for $Zn_4O(FMA)_3$ are seen in the structural parameters, especially concerning the atomic coordinates. This may be attributed to the fact that the experimental data are refined based on the fcc symmetry. The correction of the geometry of the FMA linker to a nonlinear configuration also causes the orientations of the Zn_4O nodes to be somewhat reoriented with respect to their neighboring nodes; see Figure 3.

Table 1. Optimized and Experimental Structural Parameters for $M_4O(FMA)_3$

	Zn	Zn	Cd
property	PBE–GGA	expt[a]	PBE–GGA
cryst syst	cubic	cubic	cubic
space group	*P*23 (No. 195)	*Fm*$\bar{3}$*m* (No. 225)	*P*23 (No. 195)
atoms/cell	280	70	280
a (Å)	21.8056	21.639(3)	21.9329

[a] Experimental data from ref 4.

Table 2. Selected Geometric Parameters [Bond Lengths (Å) and Angles (deg)] for $M_4O(FMA)_3$ (M = Zn, Cd) at Their Equilibrium Volumes[a]

M	C1–C2 (Å)	C2–C2 (Å)	C–O1 (Å)
Zn	1.485 ⟨1.832⟩	1.342 ⟨1.065⟩	1.276–1.279 ⟨1.249⟩
Cd	1.485–1.492	1.342	1.272–1.285
M	C2–H (Å)	M–O1 (Å)	M–O2 (Å)
Zn	1.090 ⟨0.931⟩	1.963–1.987 ⟨1.945⟩	1.971–1.977 ⟨1.988⟩
Cd	1.091	2.180–2.300	2.166–2.186
M	O1–M–O2 (deg)	M–O2–M (deg)	C1–O1–M (deg)
Zn	109.01–113.01 ⟨110.74⟩	108.03–110.87 ⟨109.47⟩	127.77–132.13 ⟨133.77⟩
Cd	85.26–126.53	105.25–113.92	99.89–142.91
M	O1–C1–O1 (deg)	O1–C1–C2 (deg)	C1–C2–C2 (deg)
Zn	126.33–126.95 ⟨121.52⟩	115.45–117.82 ⟨102.35⟩	121.81–122.35 ⟨73.10⟩
Cd	122.45–127.88	113.97–119.68	121.43–123.85

[a] The data within ⟨⟩ are derived from experimental data, and the data without ⟨⟩ are from the present structural optimization.

The optimized bond lengths and angles for both $Zn_4O(FMA)_3$ and $Cd_4O(FMA)_3$, together with those based on the experimentally reported structure for $Zn_4O(FMA)_3$, are listed in Table 2. The differences are depicted in Figure 3, which shows the atomic arrangements based on experimental and computed data. Apart from the obvious differences in the organic linker, which was incompletely characterized experimentally, there are notable changes within the optimized nodes, and in the relative positions and orientations of the nodes, compared with the experimentally data. The bond distances and angles within the linker are now within the normal range.

The results clearly demonstrate that structural optimization based on the computational method can be an indispensable tool to resolve the details of crystal structures for large multicomponent systems having complex structural frameworks when there are ambiguities or uncertainties in experimentally available structural data. State-of-the-art computational hardware and software are now available so that poor-resolution experimental data on unexplored MOFs can be supplemented with computational simulations to establish more reliable structural parameters and other properties.

The agreement between the computed structure and experimental data may be assessed by comparing the predicted powder X-ray diffraction pattern for the computed structure with that of the experimentally determined one. Figure 4a

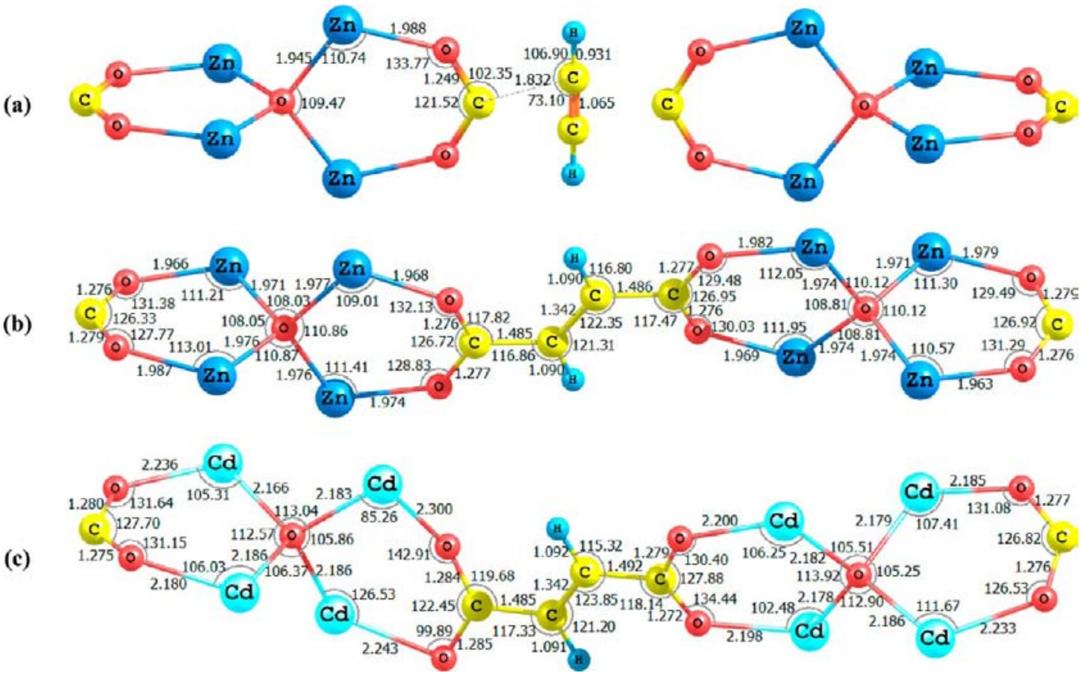

Figure 3. Optimized structural parameters [bond lengths (Å) and bond angles (deg)] for $Zn_4O(FMA)_3$ from the experimental data and calculated results in parts a and b, respectively, and those for $Cd_4O(FMA)_3$ in part c. The fragment shown in part a has local D_{2h} symmetry as a consequence of the $Fm\bar{3}m$ 3D network of $Zn_4O(FMA)_3$. In part b, an approximate C_2 local symmetry is seen.

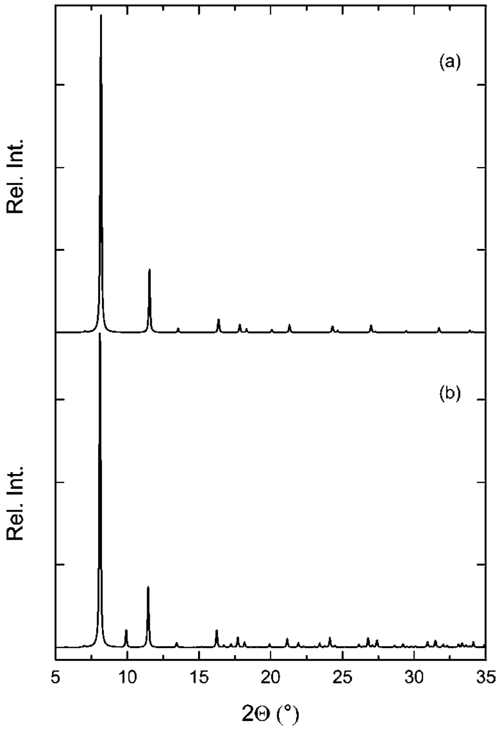

Figure 4. Simulated powder X-ray diffraction pattern (λ = 1.54056 Å) for $Zn_4O(FMA)_3$ based on (a) the structure data given in the CIF file of the single-crystal X-ray diffraction structure determination, refined in space group $Fm\bar{3}m$ (No. 225) and (b) the computationally predicted structure in this work, belonging to space group $P23$ (No. 195).

shows the simulated powder X-ray diffraction pattern based on the experimentally available[4] single-crystal X-ray crystallographic data (using the CIF file provided in the SI). Figure 4b shows the simulated powder X-ray diffraction pattern based on the optimized solid-state structure presented in this work. In general, the major characteristics of the X-ray diffraction patterns are very similar, even though some small differences arise, mostly from low-intensity signals that arise because of lowering of the symmetry. The experimental powder diffraction pattern is found in the Supporting Information of ref 4. Most of the new signals in Figure 4b (those above 2θ = 15°) are too weak to be experimentally discernible above the noise level. The new peak at 2θ = ca. 10° is entirely absent in the powder diffraction pattern of the as-synthesized sample but may be discerned in the patterns of CH_2Cl_2-exchanged and -activated guest-free samples (Supporting Information of ref 4). We conclude that the predicted pattern based on our computation is in good agreement in the experiment and that the computations give a better description of the actual local linker structure. This is of importance for the following discussions of the bonding, electronic structure, and optical properties of $Zn_4O(FMA)_3$.

C. Electronic Structure. As stated before, the computed structure of $M_4O(FMA)_3$ has sc symmetry $P23$ (No. 195) with 26 types of crystallographic positions (i.e., the 280 atoms in the unit cell were separated into 26 types on the basis of crystallographic symmetry). These include four types of M, 10 types of O, eight types of C, and four types of H. Many of these will have almost identical chemical environments because they arise from the same atoms in the MOF building blocks; this is, as expected, reflected in the partial density of states (PDOS) plots and structural data. Therefore, the discussions to follow will be based on the atom types and the numbering scheme that is given in Figure 2.

The total density of states (TDOS) and PDOS at the equilibrium volume for $M_4O(FMA)_3$ are displayed in Figure 5. (The detailed TDOS and PDOS information in the sc symmetry $P23$ (No. 195), including each of the crystallo-

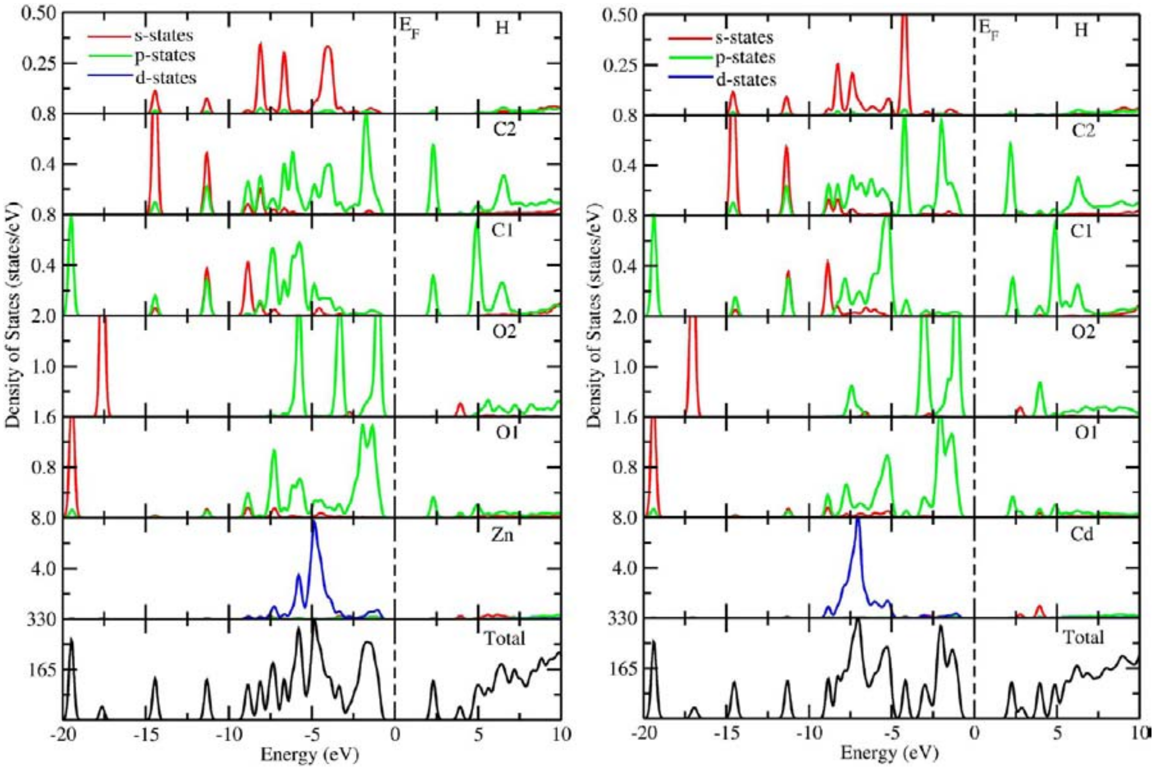

Figure 5. Calculated TDOS and PDOS for $M_4O(FMA)_3$ (M = Zn, left; Cd, right) in the sc symmetry *P*23 (No. 195). The plots are simplified according to the similarity of specific crystallographically independent atoms as discussed in the text. The atom-labeling scheme is shown in Figure 2.

graphically independent sites for each atom type, is provided in the SI.) From the DOS data, it is apparent that $Zn_4O(FMA)_3$ and $Cd_4O(FMA)_3$ have nonmetallic behavior with band-gap, E_g, values of 3.179 and 3.112 eV, respectively. These values are slightly smaller than that for MOF-5 (3.4−3.5 eV).[69,73,74] This shows that MOF band gaps can be altered through simple adjustments of the linkers in the reticular MOF series. This may be of crucial importance when MOFs are considered as candidates for applications in semiconductor devices or optoelectronics.

It is an interesting observation to note that the band gap is unaffected by the metal (M = Zn, Cd) in $M_4O(FMA)_3$. This implies that the degree of localization or delocalization of valence electrons of the M atom or the changes in the bonding interaction between M and O will not significantly affect the band-gap value of the $M_4O(FMA)_3$ materials. This is in agreement with our recent studies of members of the M-IRMOF-1 (including MOF-5), M-IRMOF-10, M-IRMOF-14, and M-IRMOF-993 series (M = Zn, Cd, alkaline-earth metals).[69−72,75] All of these metal ions are divalent and closed-shell with no possibilities for spin-state differences. Scheme 1 summarizes the calculated band gaps for the Zn-MOFs in the series addressed by us so far. It is evident that the band-gap values are quite dependent on the distance between the nodes in the MOF materials, with these distances being quite similar for IRMOF-1 and IRMOF-993. However, the rather different band-gap values seen for IRMOF-10 and IRMOF-14 (which have about the same intermodal distances), and the midrange band-gap position of $Zn_4O(FMA)_3$, which has the shortest linker of them all, suggest that other linker properties, possibly related to the size of the aromatic π system of the linker, may also play a role.

DFT-calculated band-gap values tend to be generally lower than corresponding experimentally determined values; this is intrinsically related to certain DFT limitations, namely, not taking into account the discontinuity in the exchange-correlation potential.[76] The so-called scissor operator[77] Δ can be introduced to overcome this discrepancy. In the following, we will briefly discuss and compare theoretical and experimental band-gap values for $Zn_4O(FMA)_3$ and make comparisons with the calculated data for the hypothetical $Cd_4O(FMA)_3$ and their corresponding bulk binary oxides, as well as selected MOFs for which some experimental band-gap data are available (Table 3). There is a notable discrepancy between the 3.18 eV band-gap estimate in this work and a recent calculation of 4.55 eV on the same system (for which no structural information was given);[19] it is not clear what the source of the discrepancy might be, but the different Siesta code and other basis sets were used. Our present and past results have been consistently obtained using the CASTEP code. Whereas our calculated band-gap values for $M_4O(FMA)_3$ (M = Zn, Cd) are essentially independent of M, the experimental band-gap values for the corresponding binary oxides are quite different. In particular, the band gap of CdO is ca. 1 eV smaller than that of $Cd_4O(FMA)_3$, whereas the band gaps of ZnO and MOF-5 are about 0.2−0.3 eV higher than that of $Zn_4O(FMA)_3$. This shows clearly that there is no one-to-one correspondence between the band-gap values of the IRMOFs and their respective binary oxides. The origin of band-gap formation in MOFs must therefore be different from that in binary oxides, which suggests that band gaps in the isoelectronic systems under investigation primarily originate from the linkers rather than from the cornerstone metal ions. Importantly, if detailed information about the size and origin of band gaps in MOFs is

Table 3. Calculated Band-Gap Values for $M_4O(FMA)_3$ from CASTEP Calculations and Reported Experimental and Theoretical Band-Gap Values for Zn-MOFs, ZnO, and CdO

material	linker	theor E_g (eV)	expt E_g (eV)
$Zn_4O(FMA)_3$	fumarate	3.179[a,b]	4.13[19]
		4.55[c,19]	
$Cd_4O(FMA)_3$	fumarate	3.112[a,b]	
MOF-5 (IRMOF-1)	benzene-1,4-dicarboxylate	3.4−3.5[b,69]	3.4−3.5[73,74]
		3.55[c,19]	3.80[19]
IRMOF-8	naphthalene-2,6-dicarboxylate	2.91[c,19]	3.27[19]
IRMOF-9[d]	biphenyl-4,4′-dicarboxylate	3.00[c,19]	3.42[19]
IRMOF-10	biphenyl-4,4′-dicarboxylate	2.93[b,70]	
IRMOF-14	pyrene-2,7-dicarboxylate	2.5[b,71]	
IRMOF-993	anthracene-9,10-dicarboxylate	3.59[b,72]	
UTSA-38[d]	naphthalene-2,6-dicarboxylate		2.85[78]
ZnO-w/-z			3.455/3.300[79]
CdO			2.16 ± 0.02[80]

[a] This work. [b] Calculated using the CASTEP code. [c] Calculated using the Siesta code. [d] Interpenetrated MOF network.

desired, it is advisable to perform carefully conducted calculations.

D. Energy of Formation Considerations. Information about formation energies constitute a means to establish whether theoretically predicted phases are likely to be stable, and such data may also serve as a guide to evaluate possible synthesis routes. For exploration of the thermodynamic feasibility of assembling these materials from the elements (eq 1), we have computed the total energies for C ($R\bar{3}m$), O_2 ($P4/mmm$), H_2 ($P4/mmm$), Zn ($P6_3$/mmc), and Cd ($P6_3$/mmc) in their ground-state structures with full geometry optimization. The reaction energies for MOF formation (Table 4) were calculated from the difference in the total energy between the products and reactants involved. The results establish unambiguously that eq 1 depicts highly exothermic reactions for the experimentally synthesized $Zn_4O(FMA)_3$ as well as for the analogous, yet hypothetical, $Cd_4O(FMA)_3$. Both are predicted to be rather stable phases, which, of course, is supported by the fact that $Zn_4O(FMA)_3$ is experimentally available.

Table 4. Calculated Formation Energies (ΔE; kJ mol^{-1}) According to Equation 1 for $M_4O(FMA)_3$ (M = Zn, Cd)

	Zn	Cd
ΔE (kJ mol^{-1})	−79.36	−69.51

$$8M + 13O_2 + 24C + 6H_2 \rightarrow M_8O_{26}C_{24}H_{12}$$
$$[M_4O(FMA)_3,\ M = Zn, Cd] \qquad (1)$$

Interestingly, the estimated formation energy of $Zn_4O(FMA)_3$ (−79.36 kJ mol^{-1}) is considerably more negative than that of MOF-5 (−46.02 kJ mol^{-1}). This might indicate that $Zn_4O(FMA)_3$ will form with greater ease than MOF-5. The estimated formation energy of the hypothetical heavier congener $Cd_4O(FMA)_3$ (−69.51 kJ mol^{-1}) is also more negative than that of MOF-5, indicating high stability and good opportunities for it to be experimentally accessible. Of course, under real experimental conditions, it may be possible to form other stable phases, even ones that may have lower enthalpies of formation than the investigated phases. After all, our energy minimization procedure specifically addressed the experimentally known $Zn_4O(FMA)_3$ geometry and topology.

E. Characteristics of Chemical Bonding. We have described in great detail how the bonding interactions in the M-IRMOF-1[69,75] and M-IRMOF-10[70] series can be analyzed and understood using a number of different approaches. More recently, the M-IRMOF-14[71] and M-IRMOF-993[72] series were subjected to the same scrutiny but in lesser descriptive detail. Similarly, consistent descriptions of the bonding features of $M_4O(FMA)_3$ (M = Zn, Cd) may be obtained from PDOS, charge density/transfer, ELF,[48−51] and BOP/Mulliken population analyses. The case of $Zn_4O(FMA)_3$ is used to analyze the chemical bonding; because there are only minor differences between Zn and Cd, the details for $Cd_4O(FMA)_3$ are given in the SI.

The distribution of various electronic states in the valence band (VB) as well as the conduction band (CB) of $Zn_4O(FMA)_3$ can be characterized from analysis of its PDOS, shown in Figure 5, which has already been briefly commented on. The d and s states of the Zn and H atoms, respectively, contribute dominantly to the VB. There is also noticeable contribution from the s and p states of the C and O atoms to the VB.

Charge density/transfer and ELF plots for $Zn_4O(FMA)_3$ are depicted in Figure 6. The charge density plot (Figure 6a) shows that the organic linker is a molecule-like subunit $O_2CCH{=}CHCO_2$ with normal covalent C−C, C−H, and C−O bonds. The charge densities in Figure 6a show that the charges are spherically distributed at the Zn and O sites, characteristic for systems having ionic interactions; this is further corroborated by the fact that there is no noticeable charge density distributed between the Zn and O atoms. The charge-transfer contour ($\Delta\rho$) plot in Figure 6b allows visualization of how electrons are redistributed in a particular plane in this compound compared to free atoms due to the formation of chemical bonds. It is evident that electrons are transferred from Zn to O but not entirely in an isotropic fashion. The anisotropic charge transfer from Zn to O indicates ionocovalent bonding between these atoms with a predominant ionic contribution. The nonspherical electron distribution between neighboring C, H, and O atoms together with the charge transfer between these atoms indicates strong covalent bonding. In Figure 6c, the small value of the ELF distribution between Zn and O and the small value of ELF at Zn (partially due to the presence of d electrons from Zn), along with a spherically symmetric distribution, indicate the predominant ionic bonding between Zn and O. The ELF distribution at O is polarized toward Zn, indicating small directional bonding (covalency) between Zn and O. To summarize the findings, $Zn_4O(FMA)_3$ is constructed from molecular linker subunits, bonded by normal C−H, C−C, and C−O covalent or polar covalent bonds. The bonding between Zn and O is mainly ionic but admixed with partial covalent character. Slightly diminished covalency and more ionicity is seen in the Cd−O bonds (see the SI for details).

BOP values were calculated on the basis of Mulliken population analysis.[81] A high BOP value indicates a strong covalent bond, while a low BOP value indicates an ionic or nonbonding interaction. The complete calculated BOP values

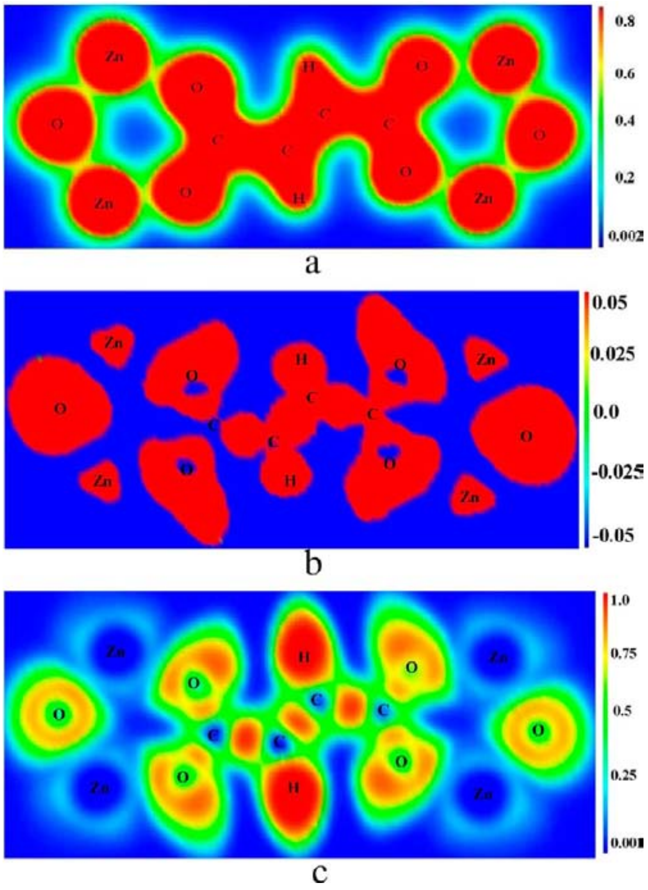

Figure 6. Calculated charge density (a) and charge transfer (b) (both in units of e $Å^{-3}$) and ELF (c) plots for $Zn_4O(FMA)_3$ in the (110) plane.

are shown in Table S2 in the SI. BOP values for the M−O bonds in the two MOFs are in the range 0.27−0.30 for M = Zn and 0.20−0.23 for M = Cd. Again, a predominant ionic character is seen in the M−O bonds with a slight decrease in the covalent character from Zn to Cd. The calculated Mulliken effective charges (MECs) are also reported in Table S2 in the SI. The MEC values are $+1.26|e|$ for both Zn and Cd. The O2 atom in the M_4O node has approximately a single unit of negative charge ($-1.04|e|$ for M = Zn and $-1.01|e|$ for M = Cd), which indicates that the four M atoms together have transferred a charge corresponding to one electron to the central O2. The O1 atoms in the FMA linker bear negative charges (-0.63 for M = Zn and $-0.64|e|$ for M = Cd), indicating that there is partial electron transfer from M to O1.

In summary, the M−O bonds in the nodes of $M_4O(FMA)_3$ (M = Zn, Cd) have predominant ionic character similar to that present in the binary oxides (MO), whereas the C−H, C−O and C−C bonds in the linkers have covalent interactions. The analyses based on charge density/transfer, ELF, and BOP/Mulliken population analyses give a consistent view of the bonding in $M_4O(FMA)_3$ (M = Zn, Cd) and agree with the situation that we have described in MOF-5,[69] the M-IRMOF-1 series,[75] the M-IRMOF-10 series,[70] the M-IRMOF-14 series,[71] and the M-IRMOF-993 series.[72]

F. Band Structures and Optical Properties. The recent report on the semiconducting behavior[82,83] of MOFs has triggered intense research in this area including the synthesis and characterization of various semiconducting MOFs with the aim of developing new materials for optoelectronic applications. In this aspect, the optical properties for $M_4O(FMA)_3$ are of particularly interest. Studies of the optical properties of MOFs are also of fundamental importance because these properties not only depend on the occupied and unoccupied parts of the electronic structure but also carry information about the character of the bands.

The central quantity of the optical properties is the dielectric function $\varepsilon(\omega)$, which describes the features of linear response of the system to electromagnetic radiation, which again governs the propagation behavior of radiation in the medium. Here we have considered $\varepsilon(\omega)$ connected to the interaction of photons with electrons; i.e., phonon contributions are not considered. Its imaginary part $\varepsilon_2(\omega)$ can be derived from interband optical transitions between the occupied and unoccupied bands including appropriate momentum matrix elements to take care of the selection rules, and its real part $\varepsilon_1(\omega)$ can be derived from $\varepsilon_2(\omega)$ by the Kramer−Kronig relationship.[52] The real part of $\varepsilon(\omega)$ in the limit of zero energy (infinite wavelength) equals the square of the refractive index $n(\omega)$. All of the frequency-dependent linear optical properties, such as refractive index $n(\omega)$, absorption coefficient $\alpha(\omega)$, optical conductivity $\sigma(\omega)$, reflectivity $R(\omega)$, and electron energy-loss spectrum $L(\omega)$ can be deduced from $\varepsilon_1(\omega)$ and $\varepsilon_2(\omega)$.[52]

CASTEP calculations were done to estimate the optical properties of $M_4O(FMA)_3$ (M = Zn, Cd), and the results from the optical calculations are shown in Figure 7. It is immediately seen that the optical properties and characteristic peaks are quite similar for Zn and Cd.

There are four main peaks in the $\varepsilon_2(\omega)$ plot (Figure 6a) of $Zn_4O(FMA)_3$ at ca. 5.02, 8.54, 12.06, and 14.71 eV, and all of these four peaks have rather strong intensities. The characteristic peaks of Cd are similar to these in position as well as appearance. From the real part of dielectric function, $\varepsilon_1(\omega)$ (Figure 6a), the value of the refractive index $n(\omega)$ at infinite wavelength is estimated at 1.2489 (Zn) and 1.2684 (Cd). This is quite similar to MOF-5 (1.25).[69] At low photon energies (0−3.15 eV), the imaginary part $\varepsilon_2(\omega)$ is zero, which is consistent with the estimated band-gap values for $M_4O(FMA)_3$.

The reflectivity spectrum (Figure 6b) of $Zn_4O(FMA)_3$ shows sharp peaks at 4.78, 7.95, 12.00, and 15.14 eV. The first and last peaks have relatively strong intensities. The two low-energy peaks mainly arise from Zn(3d) → C/O(2p) and H(1s) → C/O(2p) interband transitions. Similar features are seen for Cd. The reflectivity approaches zero when the energy exceeds 25 eV for both Zn and Cd. The values of reflectivity at infinite wavelength are 0.0121 (Zn) and 0.0142 (Cd). The values fit with the general behavior of the reflectivity of MOFs that we have considered so far[69−72,75] in that they have much smaller reflectivity values in the visible spectrum range than do common inorganic solids. This may prove to be an advantage for using MOFs in optoelectronic devices (such as solar cells and light-emitting diodes), where low reflectivity is desired.

$Zn_4O(FMA)_3$ has a finite value of the refractive index $n(\omega)$ (Figure 6c) in the range 3.15−25 eV. The extinction coefficient $k(\omega)$ (the imaginary part of the complex refractive index) shows four peaks at 5.15, 8.81, 12.12, and 14.95 eV. Similar characteristics are seen for $Cd_4O(FMA)_3$. The optical conductivity $\sigma(\omega)$ plot of $Zn_4O(FMA)_3$ is shown in Figure 6d. The real part of $\sigma(\omega)$ has four peaks at 5.11, 8.95, 12.24, and 14.79 eV. The characteristics of the main peaks are similar for $Cd_4O(FMA)_3$.

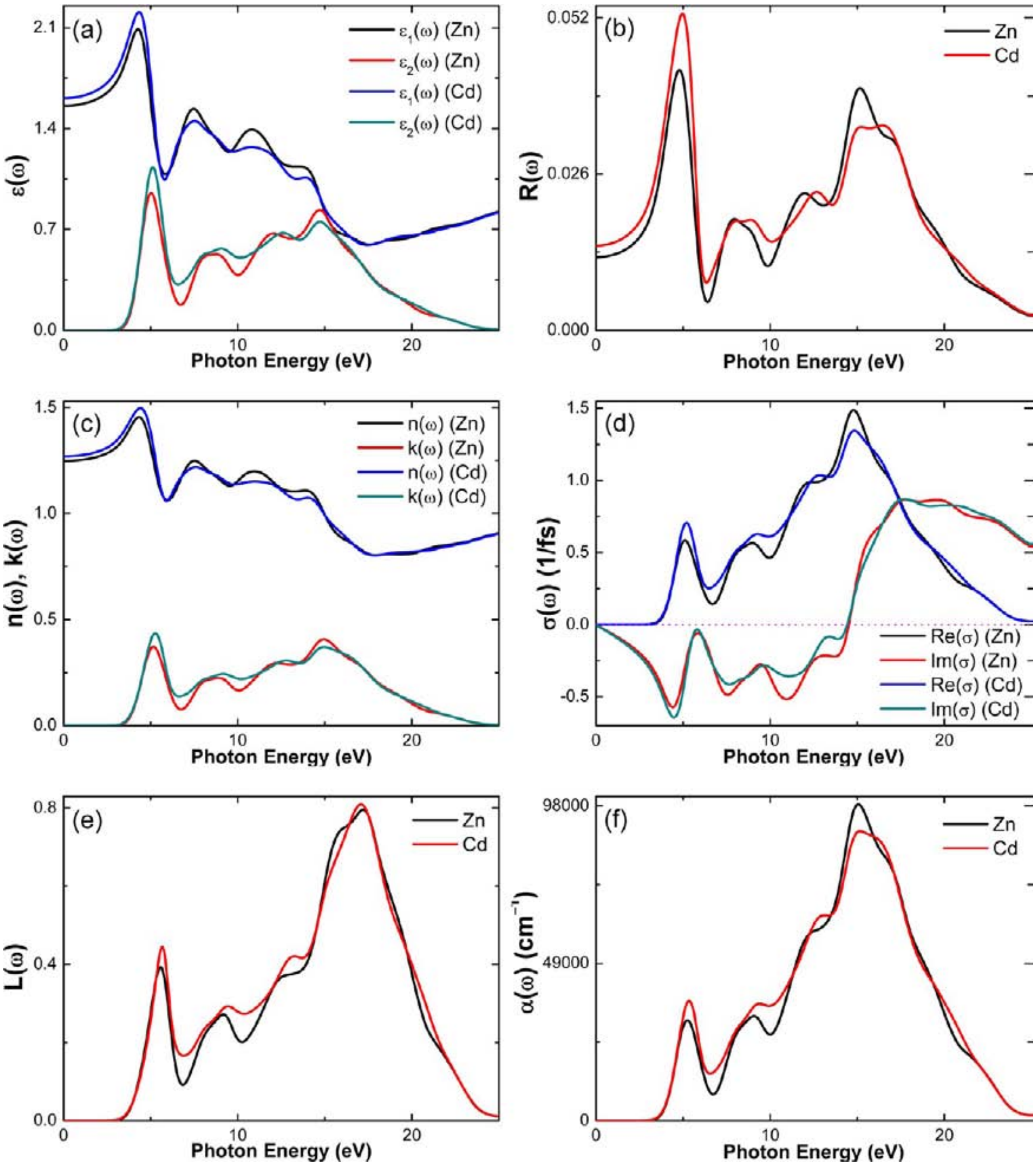

Figure 7. Calculated optical spectra for $M_4O(FMA)_3$ (M = Zn and Cd): (a) dielectric function $\varepsilon(\omega)$, (b) reflectivity $R(\omega)$, (c) refractive index $\mathbf{n}(\omega)$; extinction coefficient $\mathbf{k}(\omega)$, (d) optical conductivity $\sigma(\omega)$, (e) energy loss function $L(\omega)$, and (f) absorption coefficient $\alpha(\omega)$.

The electron energy-loss function $L(\omega)$ (Figure 6e) is an important optical parameter describing the energy loss of a fast electron traversing in a certain material. The peaks in the $L(\omega)$ spectra represent the characteristics associated with the plasma resonance. Above the plasma resonance, the material is a dielectric $[\varepsilon_1(\omega) > 0]$, and below, the material behaves like a metallic compound in some sense $[\varepsilon_1(\omega) < 0]$. In addition, the peaks in the $L(\omega)$ spectra overlap with the corresponding trailing edges in the reflection spectra. The peak in the $L(\omega)$ of $Zn_4O(FMA)_3$ at 5.54 eV corresponds to the reduction in $R(\omega)$. Three more plasma frequencies are found at ca. 9.18, 12.94, and 17.18 eV. The main features in the $L(\omega)$ spectrum of $Cd_4O(FMA)_3$ are rather similar.

Finally, $Zn_4O(FMA)_3$ has an absorption band [$\alpha(\omega)$; Figure 6f] ranging from 3.15 to 30 eV, which exhibits four peaks at ca. 5.25, 9.07, 12.48, and 15.06 eV. The main characteristics are the same for $Cd_4O(FMA)_3$. From Figure 6f, the overall observation is that the absorption spectra of M = Zn and Cd have extinction coefficients orders of magnitude smaller than those in closely related metal oxides. The smaller optical absorption in these materials will make them less useful for solar cell applications. However, the poor reflectivity and absorption in these materials may make them useful for optical devices where high transparency is required. We note that the calculated optical properties of $M_4O(FMA)_3$ are similar to those of M-IRMOF-1 in our recent contributions,[69,75] consistent with the fact that the $M_4O(FMA)_3$ and M-IRMOF-1 series have similar structural frameworks with common nodes, closely related linkers, and the same topologies.

In conjunction with the optical property calculations, the band structures of $M_4O(FMA)_3$ were calculated. The band structures are depicted in Figure 8. For the high-symmetry

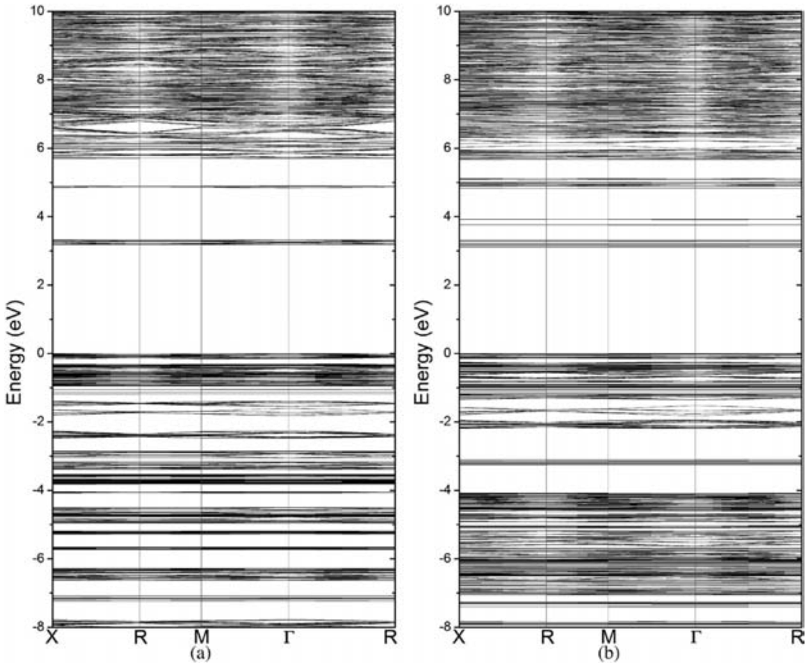

Figure 8. Electronic band structures of $M_4O(FMA)_3$ [M = Zn (a), Cd (b)]. The Fermi level is set to zero and placed in the VB maximum.

directions in the Brillouin-zone sampling, CASTEP automatically chose the **X−R−M−Γ−R** *k* path for the sc symmetry [*P*23 (No. 195)] of $M_4O(FMA)_3$. From Figure 8, it is clear that the bands at the VB maximum and CB minimum are flat and dispersionless, which makes it impossible to unequivocally identify whether the band gap is direct or indirect. This is a typical feature of the MOFs that we have investigated so far.[69−72,75] This implies that the effective mass of carriers will be high and, hence, the carrier mobility will be low. As a result, even if carriers are introduced by doping, it might be difficult to introduce sufficient electrical conductivity to use them for electrical applications.

IV. CONCLUSIONS

On the basis of an improved structure of $Zn_4O(FMA)_3$, a detailed investigation was undertaken of the electronic structure, formation energy, chemical bonding, ground-state properties, and optical properties of the experimentally available material $Zn_4O(FMA)_3$ and its hypothetical heavier congener $Cd_4O(FMA)_3$. The following important conclusions are obtained:

(1) For $Zn_4O(FMA)_3$, the calculated equilibrium lattice parameter agrees well with the experimental data. Because of the less symmetrical linker, $Zn_4O(FMA)_3$ cannot exist in the high-symmetry fcc space group [$Fm\bar{3}m$ (No. 225)] but rather in the sc space group [*P*23 (No. 195)] of lower symmetry. The revised structure incorporates a realistic description of the linker unit. Thus, it is demonstrated that computational simulations may aid experiments to arrive at improved structures for complex systems.

(2) The large negative formation enthalpy of $Zn_4O(FMA)_3$ is consistent with the fact that it has already been synthesized and found to be stable.

(3) Electronic charge density/transfer, ELF, MEC, and BOP analyses shed light on the nature of the bonding interaction between the constituent atoms. The M−O bonding interaction is mainly ionic; the ionicity of the M−O bond increases and the covalency decreases from Zn to Cd.

(4) The electronic DOS and band structure studies show that the band gap for $M_4O(FMA)_3$ is ca. 3.2 eV, resulting in a nonmetallic character.

(5) The calculated optical properties of $M_4O(FMA)_3$ provide useful information for future experimental exploration. The observation of very low reflectivity and absorption over a wide energy range shows that these materials may have potential uses in hybrid solar cell applications as a buffer layer between the electrodes and inorganic active materials.

■ ASSOCIATED CONTENT

Ⓢ Supporting Information

Detailed TDOS and PDOS information in the sc symmetry *P*23 (No. 195), atomic types and positions of $M_4O(FMA)_3$, and calculated MECs and BOPs for $M_4O(FMA)_3$. This material is available free of charge via the Internet at http://pubs.acs.org.

■ AUTHOR INFORMATION

Corresponding Author

*E-mail: mats.tilset@kjemi.uio.no (M.T.), lmyang.uio@gmail.com (L.-M.Y.). Fax: +47 22855441.

Notes

The authors declare no competing financial interest.

■ ACKNOWLEDGMENTS

We gratefully acknowledge the Research Council of Norway for financial support and for computer time at the Norwegian supercomputer facilities.

■ REFERENCES

(1) *Chem. Soc. Rev.* **2009**, *38*, issue 5, special issue on MOFs.
(2) *Chem. Rev.* **2012**, *112*, issue 2, special issue on MOFs.
(3) Long, J. R.; Yaghi, O. M. *Chem. Soc. Rev.* **2009**, *38*, 1213−1214.
(4) Xue, M.; Liu, Y.; Schaffino, R. M.; Xiang, S.; Zhao, X.; Zhu, G.-S.; Qiu, S.-L.; Chen, B. *Inorg. Chem.* **2009**, *48*, 4649−4651.

(5) Wissmann, G.; Schaate, A.; Lilienthal, S.; Bremer, I.; Schneider, A. M.; Behrens, P. *Microporous Mesoporous Mater.* **2012**, *152*, 64−70.
(6) Chalati, T.; Horcajada, P.; Gref, R.; Couvreur, P.; Serre, C. *J. Mater. Chem.* **2011**, *21*, 2220−2227.
(7) Friščić, T.; Fábián, L. *CrystEngComm* **2009**, *11*, 743−745.
(8) Zhang, K.-L.; Liang, W.; Chang, Y.; Yuan, L.-M.; Ng, S. W. *Polyhedron* **2009**, *28*, 647−652.
(9) Serre, C.; Millange, F.; Surblé, S.; Férey, G. *Angew. Chem., Int. Ed.* **2004**, *43*, 6285−6289.
(10) Zhao, L.; Xu, G.-F.; Tang, J. *J. Mol. Struct.* **2010**, *979*, 160−164.
(11) Do, J.; Lee, Y.; Kang, J.; Jacobson, A. J. *Inorg. Chim. Acta* **2012**, *382*, 191−194.
(12) Lin, J.; Wu, P.; Kang, L.; Lu, C.; Meng, Q. *Solid State Sci.* **2011**, *13*, 1538−1541.
(13) Xu, C.; Guo, Q.; Wang, X.; Hou, H.; Fan, Y. *Cryst. Growth Des.* **2011**, *11*, 1869−1879.
(14) Zhu, W.-H.; Wang, Z.-M.; Gao, S. *Gaodeng Xuexiao Huaxue Xuebao* **2011**, *32*, 532−537.
(15) Xu, X.; Zhang, X.; Liu, X.; Sun, T.; Wang, E. *Cryst. Growth Des.* **2010**, *10*, 2272−2277.
(16) Michaelides, A.; Skoulika, S.; Siskos, M. G. *CrystEngComm* **2008**, *10*, 817−820.
(17) Xu, J. Y.; Hurtado, E. J.; Lobkovsky, E. B.; Chen, B. *Acta Crystallogr., Sect. E: Struct. Rep. Online* **2007**, *E63*, m2205.
(18) Chen, B.; Ma, S.; Zapata, F.; Fronczek, F. R.; Lobkovsky, E. B.; Zhou, H.-C. *Inorg. Chem.* **2007**, *46*, 1233−1236.
(19) Lin, C.-K.; Zhao, D.; Gao, W.-Y.; Yang, Z.; Ye, J.; Xu, T.; Ge, Q.; Ma, S.; Liu, D.-J. *Inorg. Chem.* **2012**, *51*, 9039−9044.
(20) Li, H.; Eddaoudi, M.; O'Keeffe, M.; Yaghi, O. M. *Nature* **1999**, *402*, 276−279.
(21) Chen, B. Personal communication.
(22) *Mercury 3.0*; The Cambridge Crystallographic Data Centre: Cambridge, U.K., 2011; available from http://www.ccdc.cam.ac.uk.
(23) Bednowitz, A. L.; Post, B. *Acta Crystallogr.* **1966**, *21*, 566−571.
(24) Coudert, F.-X.; Mellot-Draznieks, C.; Fuchs, A. H.; Boutin, A. *J. Am. Chem. Soc.* **2009**, *131*, 11329−11331.
(25) Salles, F.; Ghoufi, A.; Maurin, G.; Bell, R. G.; Mellot-Draznieks, C.; Férey, G. *Angew. Chem., Int. Ed.* **2008**, *47*, 8487−8491.
(26) Mellot-Draznieks, C. *J. Mater. Chem.* **2007**, *17*, 4348−4358.
(27) Civalleri, B.; Napoli, F.; Noël, Y.; Roetti, C.; Dovesi, R. *CrystEngComm* **2006**, *8*, 364−371.
(28) Valenzano, L.; Civalleri, B.; Chavan, S.; Bordiga, S.; Nilsen, M. H.; Jakobsen, S.; Lillerud, K. P.; Lamberti, C. *Chem. Mater.* **2011**, *23*, 1700−1718.
(29) Valenzano, L.; Civalleri, B.; Chavan, S.; Palomino, G. T.; Areán, C. O.; Bordiga, S. *J. Phys. Chem. C* **2010**, *114*, 11185−11191.
(30) Valenzano, L.; Civalleri, B.; Sillar, K.; Sauer, J. *J. Phys. Chem. C* **2011**, *115*, 21777−21784.
(31) Chavan, S.; Vitillo, J. G.; Gianolio, D.; Zavorotynska, O.; Civalleri, B.; Jakobsen, S.; Nilsen, M. H.; Valenzano, L.; Lamberti, C.; Lillerud, K. P.; Bordiga, S. *Phys. Chem. Chem. Phys.* **2012**, *14*, 1614−1626.
(32) Lee, C.; Mellot-Draznieks, C.; Slater, B.; Wu, G.; Harrison, W. T. A.; Rao, C. N. R.; Cheetham, A. K. *Chem. Commun.* **2006**, 2687−2689.
(33) Lewis, D. W.; Ruiz-Salvador, A. R.; Gomez, A.; Rodriguez-Albelo, L. M.; Coudert, F.-X.; Slater, B.; Cheetham, A. K.; Mellot-Draznieks, C. *CrystEngComm* **2009**, *11*, 2272−2276.
(34) Bennett, T. D.; Tan, J.-C.; Moggach, S. A.; Galvelis, R.; Mellot-Draznieks, C.; Reisner, B. A.; Thirumurugan, A.; Allan, D. R.; Cheetham, A. K. *Chem.—Eur. J.* **2010**, *16*, 10684−10690.
(35) Tan, J.-C.; Civalleri, B.; Lin, C.-C.; Valenzano, L.; Galvelis, R.; Chen, P.-F.; Bennett, T. D.; Mellot-Draznieks, C.; Zicovich-Wilson, C. M.; Cheetham, A. K. *Phys. Rev. Lett.* **2012**, *108*, 095502/1−095502/6.
(36) Galvelis, R.; Slater, B.; Cheetham, A. K.; Mellot-Draznieks, C. *CrystEngComm* **2012**, *14*, 374−378.
(37) Valenzano, L.; Vitillo, J. G.; Chavan, S.; Civalleri, B.; Bonino, F.; Bordiga, S.; Lamberti, C. *Catal. Today* **2012**, *182*, 67−79.
(38) Kresse, G.; Hafner, J. *Phys. Rev. B* **1993**, *47*, 558−561.
(39) Kresse, G.; Furthmüller, J. *Comput. Mater. Sci.* **1996**, *6*, 15−50.
(40) Kresse, G.; Furthmüller, J. *Phys. Rev. B* **1996**, *54*, 11169−11186.
(41) Kresse, G.; Hafner, J. *Phys. Rev. B* **1994**, *49*, 14251−14269.
(42) Perdew, J. P. In *Electronic Structure of Solids*; Ziesche, P., Eschrig, H., Eds.; Akademie Verlag: Berlin, 1991; pp 11−20.
(43) Perdew, J. P.; Burke, K.; Wang, Y. *Phys. Rev. B: Condens. Matter* **1996**, *54*, 16533−16539.
(44) Perdew, J. P.; Burke, K.; Ernzerhof, M. *Phys. Rev. Lett.* **1996**, *77*, 3865−3868.
(45) Blöchl, P. E. *Phys. Rev. B* **1994**, *50*, 17953−17979.
(46) Kresse, G.; Joubert, D. *Phys. Rev. B: Condens. Matter* **1999**, *59*, 1758−1775.
(47) Segall, M. D.; Lindan, P. J. D.; Probert, M. J.; Pickard, C. J.; Hasnip, P. J.; Clark, S. J.; Payne, M. C. *J. Phys.: Condens. Matter* **2002**, *14*, 2717−2744.
(48) Becke, A. D.; Edgecombe, K. E. *J. Chem. Phys.* **1990**, *92*, 5397−5403.
(49) Savin, A.; Becke, A. D.; Flad, J.; Nesper, R.; Preuss, H.; von Schnering, H. G. *Angew. Chem., Int. Ed. Engl.* **1991**, *30*, 409−412.
(50) Savin, A.; Jepsen, O.; Flad, J.; Andersen, O. K.; Preuss, H.; von Schnering, H. G. *Angew. Chem., Int. Ed. Engl.* **1992**, *31*, 187−188.
(51) Silvi, B.; Savin, A. *Nature* **1994**, *371*, 683−686.
(52) Ravindran, P.; Delin, A.; Ahuja, R.; Johansson, B.; Auluck, S.; Wills, J. M.; Eriksson, O. *Phys. Rev. B: Condens. Matter* **1997**, *56*, 6851−6861.
(53) Delin, A.; Ravindran, P.; Eriksson, O.; Wills, J. M. *Int. J. Quantum Chem.* **1998**, *69*, 349−358.
(54) Ravindran, P.; Delin, A.; Johansson, B.; Wills, J. M.; Eriksson, O. *Phys. Rev. B* **1999**, *59*, 15680−15693.
(55) Ravindran, P.; Delin, A.; Johansson, B.; Eriksson, O.; Wills, J. M. *Phys. Rev. B* **1999**, *59*, 1776−1785.
(56) Ravindran, P.; Fjellvåg, H.; Kjekshus, A.; Delin, A.; Eriksson, O. *Phys. Rev. B* **2002**, *65*, 064445/1−064445/19.
(57) Karazhanov, S. Z.; Ravindran, P.; Grossner, U.; Kjekshus, A.; Fjellvåg, H.; Svensson, B. G. *Solid State Commun.* **2006**, *139*, 391−396.
(58) Karazhanov, S. Z.; Ravindran, P.; Vajeeston, P.; Ulyashyn, A.; Finstad, T.; Fjellvåg, H. *Phys. Rev. B* **2006**, *76*, 075129/1−075129/13.
(59) Brik, M. G. *J. Phys.: Condens. Matter* **2009**, *21*, 485502/1−485502/8.
(60) Chen, J.; Zhao, G.; Sun, Y.; Liu, T. *Solid State Commun.* **2010**, *150*, 897−900.
(61) Xia, Q.; Yi, J.; Li, Y.; Peng, Y.; Wang, H.; Zhou, C. *Solid State Commun.* **2010**, *150*, 605−608.
(62) Cheng, Y. C.; Wu, X. L.; Zhu, J.; Xu, L. L.; Li, S. H.; Chu, P. K. *J. Appl. Phys.* **2008**, *103*, 073707/1−073707/5.
(63) Yaghi, O. M.; O'Keeffe, M.; Ockwig, N. W.; Chae, H. K.; Eddaoudi, M.; Kim, J. *Nature* **2003**, *423*, 705−714.
(64) Ockwig, N. W.; Delgado-Friedrichs, O.; O'Keeffe, M.; Yaghi, O. M. *Acc. Chem. Res.* **2005**, *38*, 176−182.
(65) Tan, J. C.; Cheetham, A. K. *Chem. Soc. Rev.* **2011**, *40*, 1059−1080.
(66) Murnaghan, F. D. *Proc. Natl. Acad. Sci. U.S.A.* **1944**, *30*, 244−247.
(67) Birch, F. *Phys. Rev.* **1947**, *71*, 809−824.
(68) Vinet, P.; Rose, J. H.; Ferrante, J.; Smith, J. R. *J. Phys.: Condens. Matter* **1989**, *1*, 1941−1963.
(69) Yang, L.-M.; Vajeeston, P.; Ravindran, P.; Fjellvåg, H.; Tilset, M. *Inorg. Chem.* **2010**, *49*, 10283−10290.
(70) Yang, L.-M.; Ravindran, P.; Vajeeston, P.; Tilset, M. *RSC Adv.* **2012**, *2*, 1618−1631.
(71) Yang, L.-M.; Ravindran, P.; Vajeeston, P.; Tilset, M. *Phys. Chem. Chem. Phys.* **2012**, *14*, 4713−4723.
(72) Yang, L.-M.; Ravindran, P.; Vajeeston, P.; Tilset, M. *J. Mater. Chem.* **2012**, *22*, 16324−16335.
(73) Bordiga, S.; Lamberti, C.; Ricchiardi, G.; Regli, L.; Bonino, F.; Damin, A.; Lillerud, K.-P.; Bjørgen, M.; Zecchina, A. *Chem. Commun.* **2004**, 2300−2301.
(74) Alvaro, M.; Carbonell, E.; Ferrer, B.; Llabrés i Xamena, F. X.; Garcia, H. *Chem.—Eur. J.* **2007**, *13*, 5106−5112.

(75) Yang, L.-M.; Vajeeston, P.; Ravindran, P.; Fjellvåg, H.; Tilset, M. *Phys. Chem. Chem. Phys.* **2011**, *13*, 10191−10203.

(76) Perdew, J. P.; Levy, M. *Phys. Rev. Lett.* **1983**, *51*, 1884−1887.

(77) Levine, Z. H.; Allan, D. C. *Phys. Rev. B: Condens. Matter* **1991**, *43*, 4187−4207.

(78) Das, M. C.; Xu, H.; Wang, Z.; Srinivas, G.; Zhou, W.; Yue, Y.-F.; Nesterov, V. N.; Qian, G.; Chen, B. *Chem. Commun.* **2011**, *47*, 11715−11717.

(79) Karazhanov, S. Z.; Ravindran, P.; Kjekshus, A.; Fjellvåg, H.; Grossner, U.; Svensson, B. G. *J. Appl. Phys.* **2006**, *100*, 043709/1−043709/11.

(80) Jefferson, P. H.; Hatfield, S. A.; Veal, T. D.; King, P. D. C.; McConville, C. F.; Zuniga-Perez, J.; Munoz-Sanjose, V. *Appl. Phys. Lett.* **2008**, *92*, 022101/1−022101/3.

(81) Mulliken, R. S. *J. Chem. Phys.* **1955**, *23*, 1833−1840.

(82) Silva, C. G.; Corma, A.; Garcia, H. *J. Mater. Chem.* **2010**, *20*, 3141−3156.

(83) Llabres i Xamena, F. X.; Corma, A.; Garcia, H. *J. Phys. Chem. C* **2007**, *111*, 80−85.